Atmospheric Propellant Fed Hall Thruster Discharges: 0D-hybrid Model and Experimental Results

Eugenio Ferrato[1,2], **Vittorio Giannetti**[1,3], **Francesco Califano**[2], **and Tommaso Andreussi**[1,3]

[1] SITAEL - Propulsion Division, Via A. Gherardesca 5, Pisa, 56121, Italy

[2] University of Pisa - Department of Physics, Largo B. Pontecorvo 3, Pisa, 56127, Italy

[3] University of Pisa - Department of Civil and Industrial Engineering, Largo L. Lazzarino, Pisa, 56122, Italy

E-mail: eugenio.ferrato@sitael.com

Abstract. As part of on-going efforts in advancing air-breathing electric propulsion, the HT5k Hall thruster was characterized in six operating conditions, ranging from 5 mg/s to 7 mg/s of $0.56N_2 + 0.44O_2$ mass flow rate and 225 V to 300 V of discharge voltage. The cathode was operated with N_2 at mass flow rates between 0.5 mg/s and 0.7 mg/s. This paper presents a 0D-hybrid model for atmospheric propellant fed Hall thruster discharges. Verified performance ranged between 30 mN to 120 mN in thrust, 1.2 kW to 5.2 kW in discharge power, and 8% to 18% in anodic efficiency. Calibrated model comparison against experimental data resulted in a mean absolute error of 3.7% in thrust and 7.6% in discharge power.

Keywords: Air-breathing Electric Propulsion, Plasma Modeling, Monte Carlo Simulation, Very Low Earth Orbit Simulator, Air-fed Hall Thruster, Atmospheric Propellant

1. Introduction

In recent years, the utilization of Very Low Earth Orbits (VLEO, at altitudes below 250 km) gained increasing interest [1]-[3]. However, the need of a propulsion system counteracting the drag generated by orbiting through VLEO atmosphere ties the satellite lifetime to the amount of propellant stored on-board. In this regard, air-breathing Electric Propulsion (EP) is emerging as a viable concept for long-life missions in VLEO [4]-[7]. In such a concept, the electric thruster operates in air-breathing mode by means of an intake, collecting particles from the surrounding thin atmosphere and transmitting them into the thruster. The thruster then ionizes and accelerates the collected particles at high exhaust velocities, producing a thrust which compensates the drag acting on the platform. Recent air-breathing concept proposals include air-breathing ion engines [5][6], double stage Hall thrusters [7], and inductive plasma thrusters [8]. A recent review of all proposed technology concepts is provided in [9].

Understandably, a major challenge in air-breathing EP development is related to on-ground verification and reproduction of VLEO environment, characterized by atmospheric flow velocities in the order of 7.8 km/s, number densities in the 1e15 m^{-3} to 1e17 m^{-3} range, and a highly variable composition (being N_2 and O the major constituents) depending on solar and geomagnetic activities, orbital parameters, daytime and period of the year. Even if several electric propulsion devices were successfully verified with air propellant fed via laboratory gas supplies (including Hall thrusters [10] [12] [15], RF ion engines [10][13], and RF helicon inductive plasma thrusters [14]), experimental evidence of successful air-breathing operation is limited. In the study mentioned in [5], the VLEO environment was in some measure recreated by means of a laser beam detonation source, which allowed to produce hyper-thermal N_2 and O_2 flows which were collected by an intake and accelerated by a grid system. At 200 V of acceleration voltage, the tested air-breathing ion engine sustained 0.16 mA of discharge current and produced an estimated thrust of 0.13 mN. In [7], the VLEO atmospheric flow was simulated by means of an air propellant fed Hall thruster placed in front of the system intake, which however resulted in poor control and determination of the actual flow properties accepted into the air-breathing thruster prototype. The measured thrust was about 6 mN, compared to 26 mN of drag experienced by the system [7], but the thruster was operated for a very short time and with a xenon fed hollow cathode.

Together with a relatively low amount of experimental data, very few numerical models are available for air-fed and air-breathing plasma thrusters. In [16], atmospheric Hall thruster discharges are analyzed via both simplified analytical scaling laws and a two dimensional hybrid model, while theoretical investigations on the ionization processes in air-breathing plasma thrusters were performed in [17]. In [18], a global model for the operation of an air-breathing thruster is described, whereas in [19] Monte Carlo simulations of the ion and neutral flows are added to a 0D reactor model, allowing to effectively couple the intake and thruster physics. In this regard, it is apparent how a practical modelling approach capable of predicting the on-ground and in-orbit performance of air-breathing systems would greatly aid the advancement of the technology. The integration of such a model into an orbital propagator would allow to investigate optimal on-orbit thrust and power management strategies [20], thus increasing the significance of mission analyses which should be performed as part of the development process of any targeted air-breathing EP concept.

In the framework of the European Commission H2020 programme AETHER (Air-breathing Electric THrustER), operation with atmospheric propellant of SITAEL's 5kW-class HT5k Hall thruster [21] was characterized. AETHER aims at developing the first propulsion system able to maintain a spacecraft at very-low altitudes for an extended time by demonstrating, in a relevant environment, the critical functions of an air-breathing electric propulsion system, and its effectiveness in compensating atmospheric drag [22]. In this regard, characterizing the operation of an air-fed Hall thruster allows to collect relevant data to aid the design of air-breathing thrusters, and to evaluate whether an air-fed Hall thruster placed in front of the intake may be a suitable VLEO

simulator for on-ground verification of the air-breathing technology. As reported in Sec. 2, such an experimental campaign was successfully performed in November 2021 at SITAEL's premises. Based on the result obtained from the characterization test, this paper presents a hybrid-0D approach for modelling Hall thruster atmospheric plasma discharges as a compromise among accuracy, robustness and computational cost. Model formulation is derived in Sec. 3, while in Sec. 4 we report the performance achieved by the HT5k operating with $0.56N_2 + 0.44O_2$ to the anode line and N_2 to the cathode line. The experimentally demonstrated performance is then compared with the model output, showing good agreement with the test data. Based on the obtained results, in Sec. 4 we provide and discuss the model sensitivity to calibration parameters and operating condition in terms of discharge voltage, mass flow rate and inlet propellant composition.

2. Particle Flow Generator Characterization Test Campaign

The Particle Flow Generator characterization test was conducted in SITAEL's IV10 vacuum facility. The test item was a VLEO flow simulator, referred to as Particle Flow Generator (PFG) and consisting of the 5kW-class, magnetically shielded HT5k Hall thruster [21] fed with air mixture and coupled with the HC20h hollow cathode [23] fed with pure nitrogen. The test objective was to verify the discharge and thermal stability of the PFG during continuous operation with atmospheric propellant, and to collect all the necessary data to quantitatively compare the output PFG plume flow properties against a reference VLEO orbital flight scenario. Figure 1 shows the realized test setup before chamber closure. With a inner diameter of 5.4 m, an internal length of 6 m, and a pumping speed of 4.2e5 l/s for Xe, the IV10 vacuum facility was capable of ensuring pressure levels (as measured by a Leybold ITR90 pressure sensors located 3 m downstream the thruster) below 2.5e-5 mbar throughout all testing activities. During the test, the
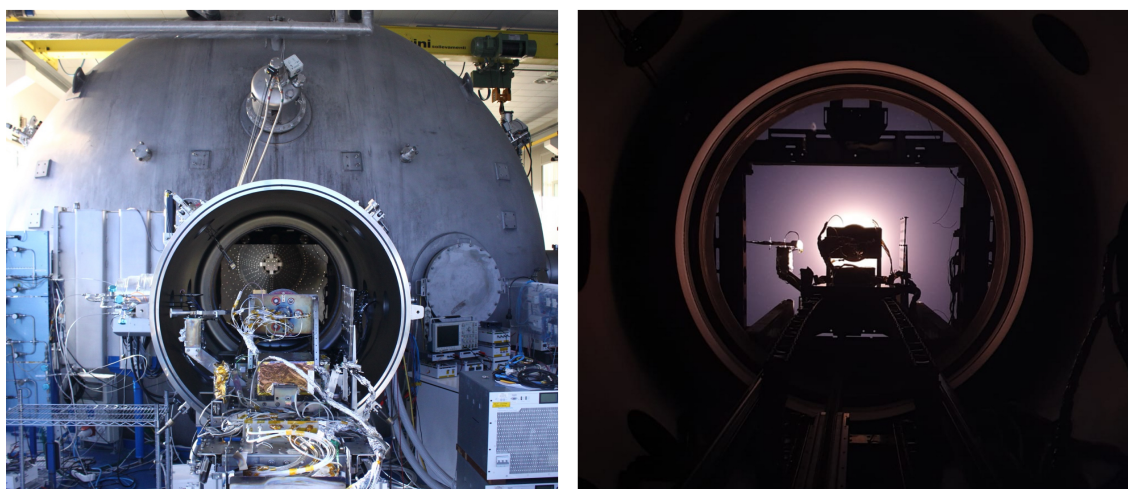

Figure 1: (a): PFG characterization test setup and IV10 vacuum facility. (b): PFG firing with air-propellant, as seen from IV10 rear view port.
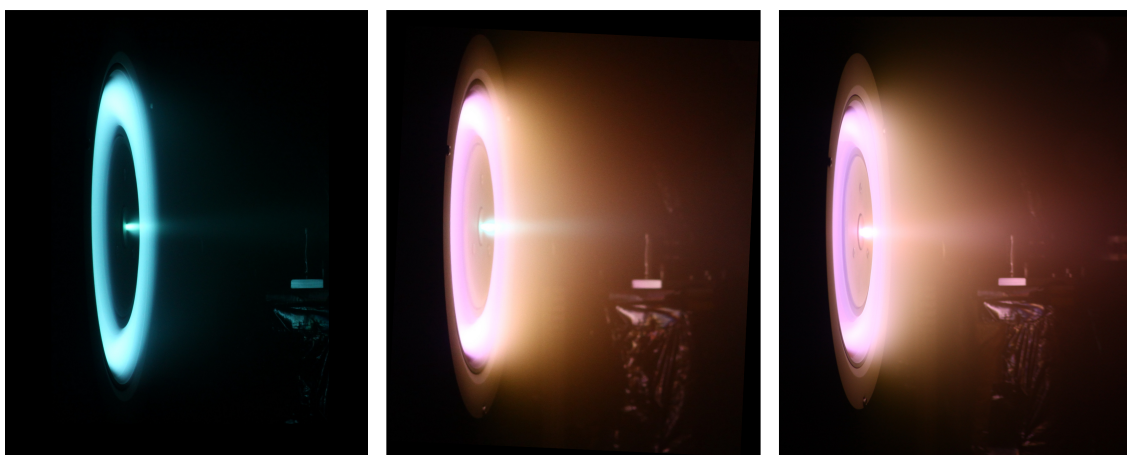
Figure 2: PFG operation at 225 V of discharge voltage with: (a) 10 mg/s Xe to anode and 1 mg/s Xe to the cathode; (b) 6 mg/s $0.56Xe + 0.44O_2$ to anode and 1 mg/s Xe to the cathode; (c) 6 mg/s $0.56N_2 + 0.44O_2$ to anode and 0.6 mg/s N_2 to the cathode.

thruster discharge circuit was supplied using a Regatron TC.P.20.500.400.S laboratory power supply, and the discharge current signal was aquired at 10 MHz frequency via a YOKOGAWA-DL850E oscilloscope. Based on the recommended practice prescribed in [24], the generated thrust was measured by means of a single axis thrust stand with a double pendulum configuration and thermal drift compensation. The thrust sensing is based on high precision load cells measuring the strain on the flexural elements with a 3σ accuracy of ±3 mN, as estimated via multiple measurements taken against a commercial HBM PW6CC3MR-3kg load cell previously calibrated against a 0.5 kg calibration mass. The thrust stand is also equipped with an internal electromagnetic calibrator, generating a reference force when requested, and internal calibration was performed at least twice a day in both thruster cold and hot conditions. Four laboratory mass flow controllers were used to feed the PFG anode and cathode lines. The Bronkhorst F-201CV-300-AAD-88-V and F-201CV-500-AAD-88V were used to respectively provide Xe and $0.56N_2+0.44O_2$ propellant mixtures to the anode, while two Bronkhorst F-201C-FAC-88-V were used to provide Xe and N_2 propellant to the cathode. The fluidic setup allowed to perform smooth propellant transitions and achieve stable thruster operation with atmospheric propellant. As shown in Figure 2, the thruster was initially ignited at 225 V of discharge voltage, 10 mg/s Xe of anode mass flow rate and 1 mg/s Xe of cathode mass flow rate. Propellant transition was at first performed on the anode line, gradually switching from 10 mg/s Xe to 6 mg/s $0.56N_2+0.44O_2$. Full atmospheric propellant operation was then achieved by providing nitrogen to the cathode line, gradually reducing the injected Xe down to 0 mg/s while increasing the N_2 mass flow up to 0.6 mg/s. From this reference operating condition, discharge voltage and mass flow rate were varied at a constant cathode to anode mass flow rate ratio of 1/10, and the thruster was successfully characterized in six different operating conditions. During the test, thermal and discharge stability was demonstrated at discharge voltages of 225V and 300 V and for $0.56N_2+0.44O_2$ injected

mass flow rate in the 5 mg/s to 7 mg/s range, resulting in discharge power between 1.2 kW and 5.2 kW, thrust between 30 mN and 120 mN, and anodic efficiency in the 8% to 18% range. The cumulative firing duration with atmospheric propellant was of 10 hrs. A reference Xe performance test, performed both before and after the air characterization, was repeatable within acquisition accuracy and showed no evidence of PFG critical damage. A stainless-steel anode was selected for this specific test. During the post-test inspection, a few regions with an altered coloration were observed over the PFG anode surface directly exposed to the atmospheric plasma discharge. This is likely due the onset of an oxidation layer over the anode, which however did not compromise the anode functionality for the short duration of the test campaign. On the other hand, no signs of chemical alterations were observed on the other thruster components.

3. Methods

3.1. 0D-hybrid Discharge Model

The current status and challenges in discharge modelling of traditional Xe-fed Hall thrusters is well reviewed in [25] and [26]. In this work, we adapt to the HT5k Hall thruster the hybrid-0D formulation presented in [19] for air-breathing EP systems.
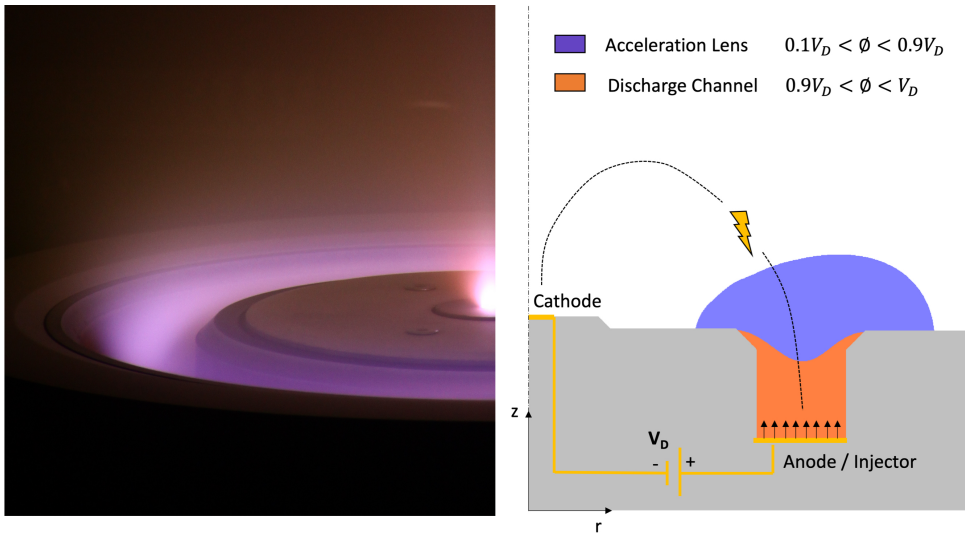

Figure 3: (a): detail of PFG firing with atmospheric propellant. (b): HT5k discharge channel and acceleration lens domain definition.

As discussed in [19], the core of the proposed hybrid model consists of the system of 0D ODE equations derived in Sec. 3.4. Each equation represents particle continuity of the s-th neutral species (N, N_2, O, O_2) or s+ singly ionized species (N^+, N_2^+, O^+, O_2^+) in the discharge channel or acceleration lens control volumes, which are respectively labeled with the subscript i and a. As indicated in Figure 3, we define the discharge channel control volume as the volume bounded by the anode injection plane, the channel insulating walls and the equipotential surface $\phi = 0.9V_D$, where V_D the voltage applied

Table 1: Neutral and Ion Flow Parameters computed by Monte Carlo methods.

Parameter	Symbol	Definition
Channel transmission	$\alpha_{s,i}/\alpha_{s+,i}$	Probability of a neutral/ion particle in the discharge channel to be accepted into the acceleration lens control volume.
Acc. lens transmission	$\alpha_{s,a}/\alpha_{s+,a}$	Probability of a neutral/ion particle in the acceleration lens to effuse/be accelerated to the external environment.
Channel residence time	$\tau_{s,i}/\tau_{s+,i}$	Mean of the neutral/ion particles residence time distribution in the discharge channel control volume.
Acc. lens residence time	$\tau_{s,a}/\tau_{s+,a}$	Mean of the neutral/ion particles residence time distribution in the acceleration lens control volume.
Escape velocity	$u_{s,a}/u_{s+,a}$	Mean of the axial velocity distribution of the neutral/ion particles effusing/being accelerated through the acceleration lens to the external environment.

between the anode and cathode electrodes, and the acceleration lens control volume as bounded by the two equipotential surfaces $\phi = 0.1V_D$ and $\phi = 0.9V_D$. Particle continuity equations solve for the s or s+ species number density n in the two control volumes and are coupled with electron energy conservation, which allows to compute the time-dependent electron temperatures $T_{e,i}$ and $T_{e,a}$. We describe neutral and ion particles dynamics through the set of parameters defined in Table 1, including particle transmission (also known as Clausing factors), mean residence time in the two thruster control volumes, and mean axial velocity of the particles leaving the thruster domain. Information on higher dimensionality is taken into account by means of a 2D magnetic/potential solver and a 3D Monte Carlo algorithm for both neutral and ion particles. The neutral Monte Carlo, discussed in Sec. 3.3, is based on the Cercignani-Lord-Lampis wall collision model [31]. The ion Monte Carlo, also discussed in Sec. 3.3, consists of a 3D Boris pusher [32] in static 2D EM fields computed by solving Ampere's and electron drift-diffusion PDEs [33], see Sec. 3.2. The modelling approach presented here relies on several approximations discussed in the following:

- Both ion and neutral dynamics are approximated as collisionless. Hence, processes such as chemical reactions and charge/momentum exchange between heavy species are neglected;

- In computing the electron mobility, electron-neutral collisions are neglected in comparison with anomalous diffusion. This is verified experimentally for the plume and acceleration regions of Hall thrusters [29], while classic collisions are the dominant electron transport mechanism near the anode injection plane. Being this a limited region of the domain, we considered negligible the impact of classic

electron collisionality on the global model solution;

- Electron pressure is neglected in solving the 2D plasma potential and, in line with a 0D approach, the plasma density is approximated as constant in each control volume;

- Due to the intrinsic limitations of a 0D approach, no information is available regarding the ionization source profile inside the thruster domain, and the ion birth location is approximated as uniform in each of the two control volumes;

- Only neutral and ion species at ground state are included, and excitation losses are accounted for in electron energy conservation by introducing an effective cost coefficient β which, together with the anomalous diffusion coefficient α_B, is a model calibration parameter.

3.2. 2D Magnetic and Potential Solver

The 2D magnetic and potential solver is implemented in the FreeFem++ [27] environment. For a given axisymmetric thruster design, we compute the applied magnetic field $B = \nabla \times A$ from the magnetic vector potential $A = A_\theta(r,z)$:

$$\int \nabla^2 A \, \mathrm{d}V = -\int \mu_r \mu_0 j_c \, \mathrm{d}V, \tag{1}$$

where we neglect the effect of plasma current density as compared to the thruster coil current density j_c. μ_0 and μ_r are the vacuum and relative to vacuum magnetic permeability and $A = 0$ is set as BC in the far field boundaries. The plasma electric potential is then computed from the applied magnetic field solution by neglecting the effect of electron pressure gradients and combining electron momentum conservation with charge continuity, resulting into the weak form

$$\int \nabla \cdot (\bar{\bar{\mu}} \cdot \nabla \phi) \, \mathrm{d}V = \int \nabla \cdot \Gamma_i / n \, \mathrm{d}V, \tag{2}$$

with Dirichlet BCs on the thruster electrodes and Neumann BC on the insulating wall surfaces. In (2), $\nabla \cdot \Gamma_i$ is the ion flux divergence and the electron mobility r-z tensor $\bar{\bar{\mu}}$ is

$$\bar{\bar{\mu}} = \mu \begin{pmatrix} \frac{1+\mu^2 B_r^2}{1+\mu^2 B^2} & \frac{\mu^2 B_r B_z}{1+\mu^2 B^2} \\ \frac{\mu^2 B_r B_z}{1+\mu^2 B^2} & \frac{1+\mu^2 B_z^2}{1+\mu^2 B^2} \end{pmatrix}, \tag{3}$$

$$\mu = \frac{e}{m_e \nu_c} \sim \frac{1}{\alpha_B B}, \tag{4}$$

being m_e the electron mass and ν_c the electron collision frequency. We assume anomalous diffusion to be the dominant electron transport mechanism, being α_B Bohm's anomalous diffusion coefficient. For sufficiently low values of electron collisionality ($\alpha_B < 1/16$), the potential solution is not impacted. On the other hand, as $\alpha_B \to \infty$ the anisotropy induced by the applied magnetic field vanishes, see Figure 4. In line with a 0D approach, in (2) we approximate $n = n(t)$ and $\nabla \cdot \Gamma_i / n \sim \kappa(t)$, where κ is a piece-wise function representing the mean ionization frequency in each control volume. At iteration 0, $\kappa = 0$
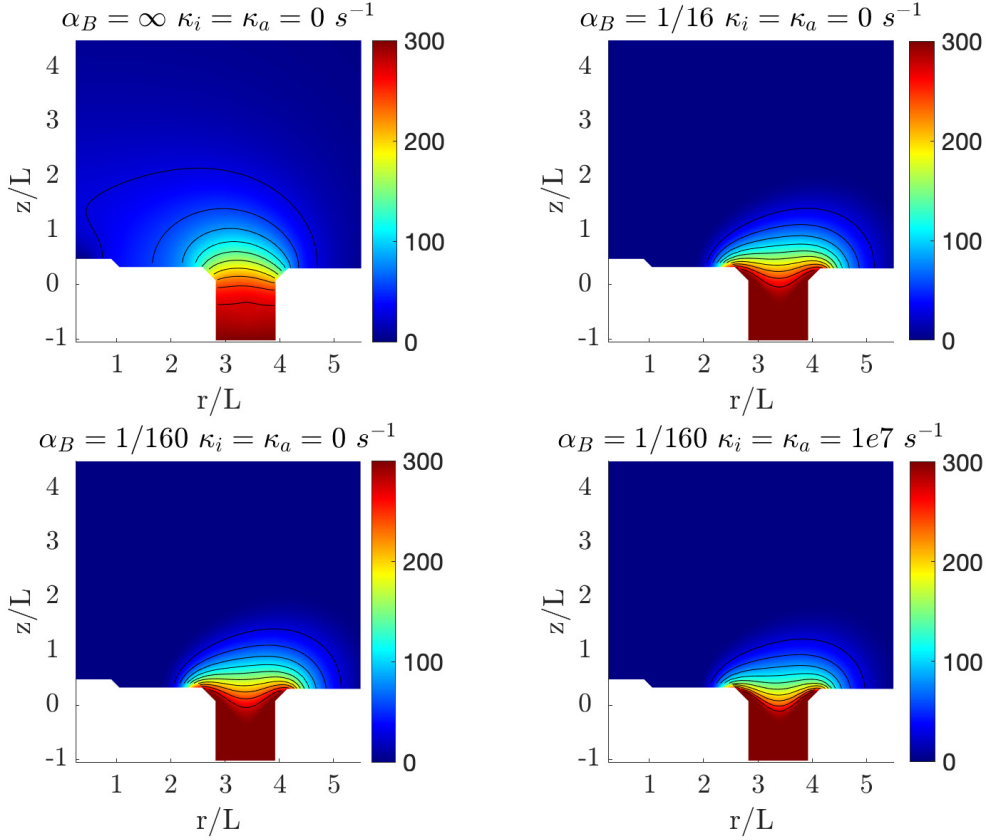
Figure 4: Impact of α_B and κ on 2D potential solution. The thruster anode potential is set at 300V. Axes are normalized against discharge channel length L.

is set everywhere in the domain. The solution obtained from 0D particle continuity and electron energy balance, see Sec. 3.4, is then used to compute a more refined κ function as

$$\nabla \cdot \Gamma_i / n \sim \kappa = \begin{cases} \kappa_i & \text{in discharge channel} \\ \kappa_a & \text{in acceleration lens} \\ 0 & \text{elsewhere} \end{cases}, \tag{5}$$

where

$$\kappa_i = \sum_{s+} \frac{n_{s+,i}}{\tau_{s+,i}} / \sum_{s+} n_{s+,i}, \tag{6}$$

$$\kappa_a = \left(\sum_{s+} \frac{n_{s+,a}}{\tau_{s+,a}} - \frac{V_i}{V_a} \sum_{s+} \frac{\alpha_{s+,i} n_{s+,i}}{\tau_{s+,i}} \right) / \sum_{s+} n_{s+,a}. \tag{7}$$

The two terms in the right-hand side of (7) represents the number of ion particles generated in the acceleration lens control volume per unit time and the number of ions transmitted per unit time from the discharge channel to the acceleration lens, being V_i / V_a the volume ratio between the two control volumes. In principle, consistent values
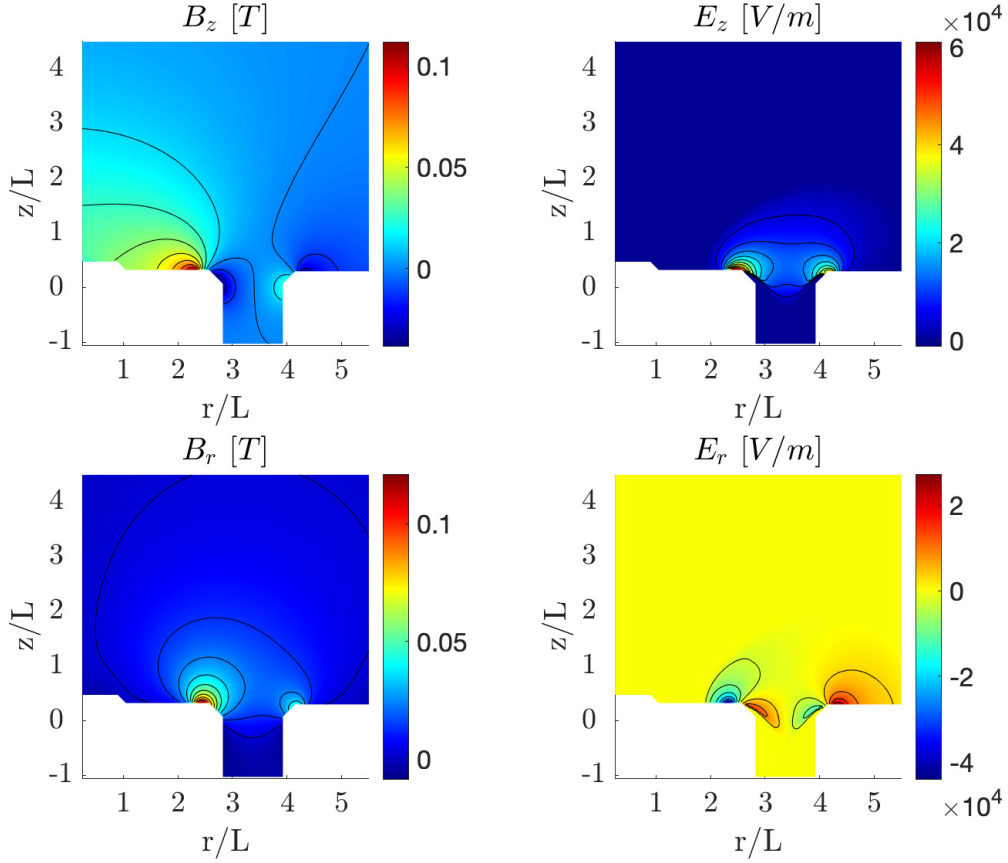
Figure 5: Output 2D magnetic and electric fields solution for the nominal HT5k coil currents and for 300V of discharge voltage. $\alpha_B = 1/126$, $\kappa_i = $ 9e4 1/s, $\kappa_a = $ 5e5 1/s, which is consistent with the steady-state solution of Figure 9. Axes are normalized against discharge channel length L.

of κ_i and κ_a should be recovered at each time step from the solutions of the 0D model and Monte Carlo simulations in an iterative process. Nevertheless, it is observed that for meaningful values of α_B, κ_i, and κ_a the output electric potential does not vary substantially. As Figure 4 shows for a reference 300 V discharge, the 2D electric potential solution is not impacted for values of κ less than 1e6 1/s and a single iteration is usually sufficient to ensure consistency with variations of less than 1% everywhere in the domain. An example of output axial/radial magnetic and electric field solutions is shown in Figure 5 for the tested thruster coil currents and an applied anode voltage of 300V.

3.3. 3D Ion and Neutral Monte Carlo

As the thruster magnetic and electric fields are computed, we proceed to extract all the parameters listed in Table 1 by running the 3D Monte Carlo algorithm for each neutral and ion species. Figure 6 provides a comparison among the computed trajectories for 1e3 N_2 and 1e3 N_2^+ particles. The initial neutral position is sampled from a uniform

distribution over the anode injection plane, and its initial velocity is sampled from a half-Maxwellian distribution ($v_{z,0} \geqslant 0$) set at anode temperature. The particle trajectory is propagated as a straight line until a collision with insulating walls or anode injection plane occurs. The updated position at collision location is then computed together with a newly sampled reflected velocity. The process is repeated until the particle escapes. An extensive review of gas-surface interaction models is provided in [30], including Maxwell, NHS and CLL scattering kernels and hard-cube, soft-cube and washboard physical models. For this algorithm, we use the CLL scattering kernel [31] for sampling the reflected velocity. We set both the anode and discharge channel wall temperature at $T_w = 800$ K. As suggested in [31], we assume a wall normal energy and tangential momentum accommodation coefficients of $\alpha_n = 1$ and $\alpha_t = 0.9$, respectively. The initial ion position is instead sampled from a uniform distribution in the two thruster control volumes, and its initial velocity is sampled from a Maxwellian distribution set at thruster wall temperature T_w. Ion trajectories are propagated in the computed 2D EM fields by means of a Boris pusher [32] with a fixed time step $\Delta t = 0.1\chi_{s+}^{-1}$, being χ_{s+} an ion frequency computed as

$$\chi_{s+} = \frac{e}{M_{s+}}\left(B_{max} + E_{max}\sqrt{\frac{M_{s+}}{2eV_D}}\right),\tag{8}$$

where M_s is the s-th species atomic/molecular mass, e is the elementary charge, V_D is the applied discharge voltage, and B_{max} and E_{max} are the maximum values of magnetic and electric field intensity in the thruster domain. The condition defining the fixed pusher time step allows to both capture the lowest ion gyroperiod in at least ten time intervals
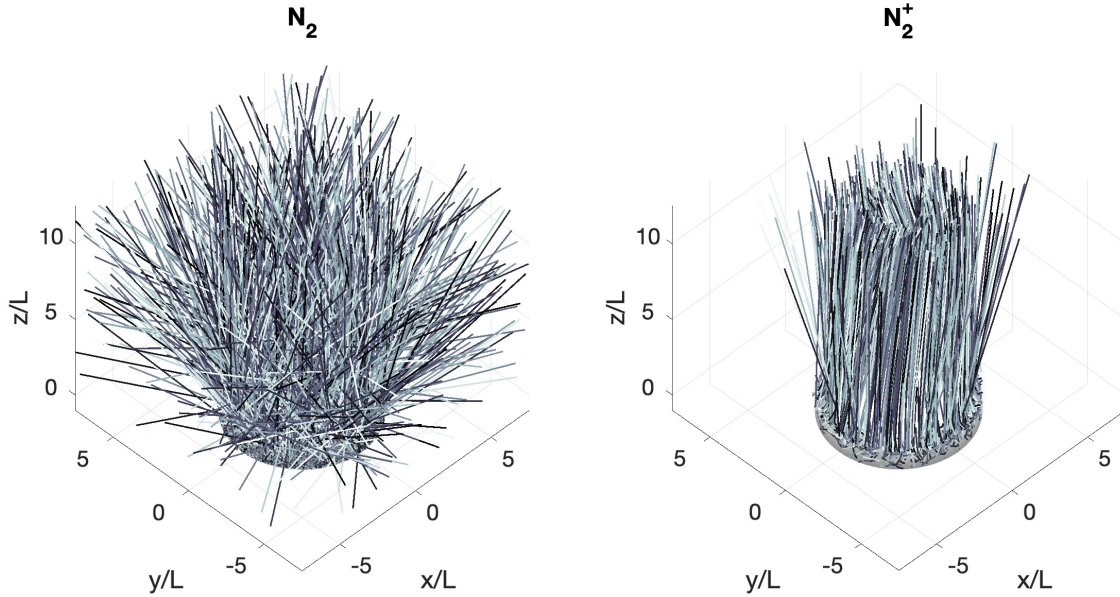

Figure 6: (a): 1e3 N_2 particles trajectory for $T_w = 800$ K. (b): 1e3 N_2^+ particles trajectory for $V_D = 300$ V. Axes are normalized against discharge channel length L.
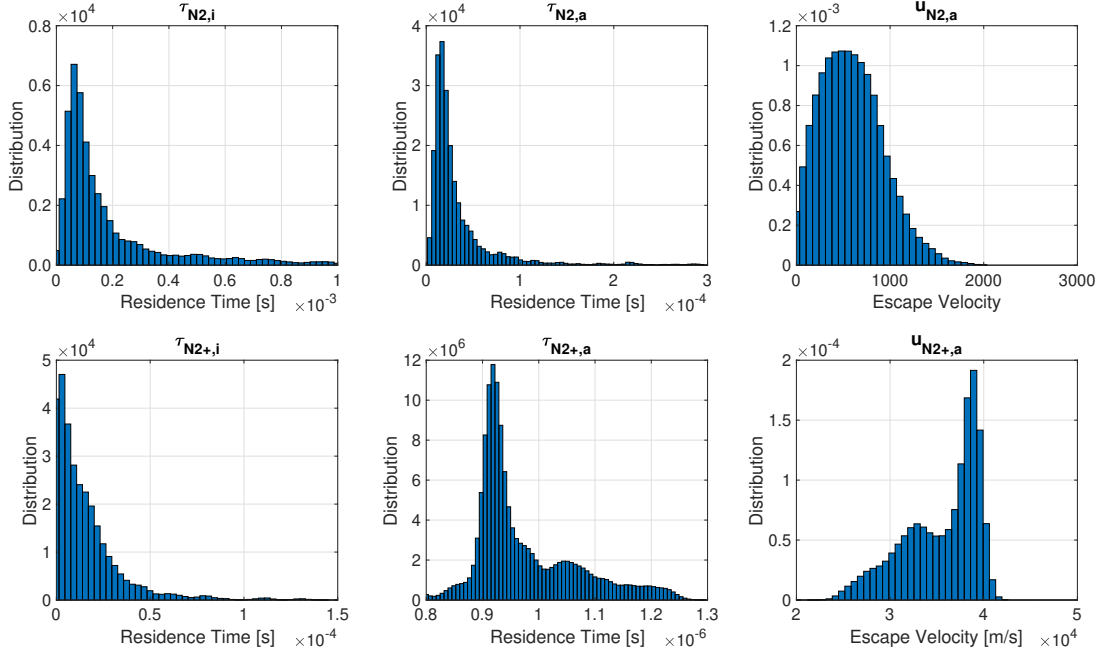
Figure 7: Neutral and Ion Monte Carlo output for 1e5 simulated N_2 and N_2^+ particles at a reference $T_w = 800$ K and $V_D = 300$ V thruster operating condition.

and, more importantly, to ensure that the distance travelled by any ion particle between each time step is at least an order of magnitude lower than V_D/E_{max}, which is itself significantly smaller that the characteristic size of the computational domain. Each ion trajectory is followed until it crosses a domain boundary, may it be an insulating wall, an electrode or the far plume region. The 3D Monte Carlo is programmed in MATLAB, and all simulations were performed via a 2.3GHz quad-core Intel i5 processor resulting into an average computation time of 0.04 s per neutral particle and 0.25 s per ion particle. As a compromise among precision and computational cost, we choose to simulate 1e5 particles for each species, estimating (with a 99.7% confidence level) a precision better than $\pm 1\%$ for all the output parameters listed in Table 2.

Table 2: Neutral/Ion Monte Carlo output for a reference $T_w = 800$ K and $V_D = 300$ V thruster operating condition. 1e5 particles were simulated for each species.

Species	α_i	α_a	τ_i [s]	τ_a [s]	u_a [m/s]
N_2	1	1	2.22e-4	2.90e-5	5.00e2
N	1	1	1.57e-4	2.46e-5	6.95e2
O_2	1	1	2.52e-4	2.98e-5	4.87e2
O	1	1	1.76e-4	2.48e-5	6.43e2
N_2^+	0.542	1	2.09e-5	9.62e-7	3.21e4
N^+	0.541	1	1.26e-5	6.79e-7	4.24e4
O_2^+	0.542	1	1.77e-5	1.02e-6	3.02e4
O^+	0.543	1	1.26e-5	7.27e-7	4.06e4

Figure 7 shows the main Monte Carlo output for 1e5 simulated N_2 and N_2^+ particles, while Table 2 reports the computed values of the parameters defined in Table 1 and inserted into the 0D continuity equations discussed in Sec. 3.4. The output is consistent with expectations, as particle escape velocity and mean residence times respectively decrease and increase with the atomic/molecular mass. Due to collisions with ceramic wall and anode injection plane, the mean residence time of the neutral particles is about one order of magnitude higher in the discharge channel as compared to the acceleration lens control volume. Neutral particle transmission is always 1 as particle injection is forced by the feeding system. On the other hand, about 46% of low-energy ions in the discharge channel are neutralized at channel walls, independently from their mass. As full ion transmission is obtained through the acceleration lens, the occurrence of neutralization at thruster walls of high-energy ions is significantly less than one in 1e5 simulated particles, which is consistent with the working principle of magnetic shielding [34].

3.4. 0D Particle Continuity and Electron Energy Balance

The 0D global model is implemented in MATLAB environment, and makes use of the built-in ODE23 solver. In the discharge channel and acceleration lens control volumes, we express ion and neutral particle continuity as

$$\frac{dn_{s,i}}{dt} = \frac{\Gamma_s}{V_i} - \frac{n_{s,i}}{\tau_{s,i}} + \frac{(1-\alpha_{s+,i})n_{s+,i}}{\tau_{s+,i}} + \dot{\omega}_{s,i} \tag{9}$$

$$\frac{dn_{s+,i}}{dt} = -\frac{n_{s+,i}}{\tau_{s+,i}} + \dot{\omega}_{s+,i}, \tag{10}$$

$$\frac{dn_{s,a}}{dt} = \frac{V_i}{V_a}\frac{\alpha_{s,i}n_{s,i}}{\tau_{s,i}} - \frac{n_{s,a}}{\tau_{s,a}} + \frac{(1-\alpha_{s+,a})n_{s+,a}}{\tau_{s+,a}} + \dot{\omega}_{s,a} \tag{11}$$

$$\frac{dn_{s+,a}}{dt} = \frac{V_i}{V_a}\frac{\alpha_{s+,i}n_{s+,i}}{\tau_{s+,i}} - \frac{n_{s+,a}}{\tau_{s+,a}} + \dot{\omega}_{s+,a}. \tag{12}$$

where $\Gamma_s = \dot{m}_s/M_s$ is the particle flux injected into the thruster, being $\dot{m}_s$ the s-th species anode mass flow rate. The four terms in the right-hand side of (9) respectively represents the inlet particle flux, flow convection, ion flow neutralized at walls, and a source/sink term $\dot{\omega}_s$. The latter is related to ionization and dissociation phenomena involving energetic electrons in the thruster discharge:

$$\dot{\omega}_{s,i} = \sum_j \nu_{s,j}k_j(T_{e,i})n_{j,i}n_{e,i}, \tag{13}$$

where $k_j(T_{e,i})$ is the electron temperature dependant reaction rate of the j-th reaction, the neutral or ionized species number density $n_{j,i}$ and electron number density $n_{e,i} = \sum n_{s+,i}$ (assuming quasi-neutrality) are the reactants of the j-th reaction, and $\nu_{s,j}$ is the stoichiometric coefficient defining the amount of species s created or destroyed in the j-th reaction. The list of reactions and related cross sections implemented in the code

are provided in Table 3 and Figure 8, respectively. As we estimated chemical reaction at walls and among neutrals, ion-electron recombination, and negative ionization to be of secondary importance as compared to electron impact reactions, these processes are not currently accounted for in the model. Nonetheless, they could easily be included as additional source/sink terms in the continuity equations.

Table 3: Review of hybrid 0D model reaction rates and reaction energies. $v_{th,e}$ is the mean of the magnitude of electron thermal velocity and σ_j is the cross section relevant to the j-th reaction.

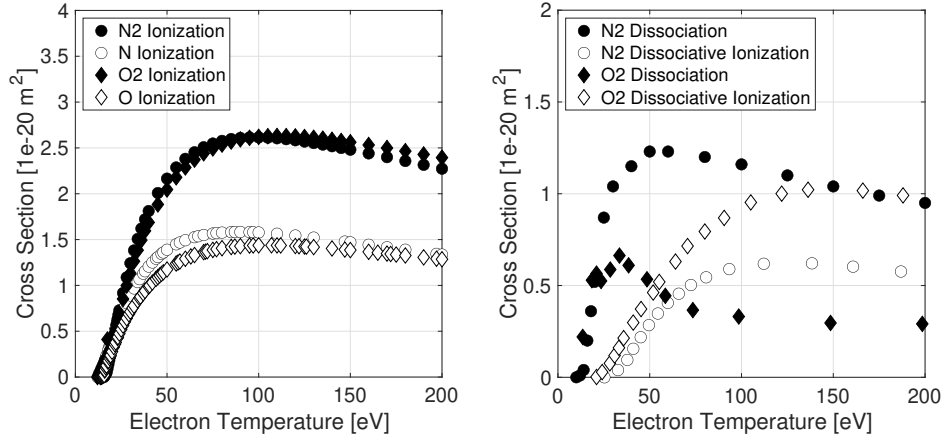| Reaction	Reaction Rate $[m^3/s]$	Energy $[eV]$	Ref.
$N_2 + e \to N_2^+ + 2e$	$k_1 = \sigma_1 v_{th,e}$	$\epsilon_1 = 15.58$	[35]
$N + e \to N^+ + 2e$	$k_2 = \sigma_2 v_{th,e}$	$\epsilon_2 = 14.53$	[36]
$O_2 + e \to O_2^+ + 2e$	$k_3 = \sigma_3 v_{th,e}$	$\epsilon_3 = 12.07$	[35]
$O + e \to O^+ + 2e$	$k_4 = \sigma_4 v_{th,e}$	$\epsilon_4 = 13.62$	[36]
$N_2 + e \to 2N + e$	$k_5 = \sigma_5 v_{th,e}$	$\epsilon_5 = 12.14$	[37]
$N_2 + e \to N^+ + N + 2e$	$k_6 = \sigma_6 v_{th,e}$	$\epsilon_6 = 26.67$	[38]
$O_2 + e \to 2O + e$	$k_7 = \sigma_7 v_{th,e}$	$\epsilon_7 = 7.360$	[37]
$O_2 + e \to O^+ + O + 2e$	$k_8 = \sigma_8 v_{th,e}$	$\epsilon_8 = 20.98$	[38]

Figure 8: N2, N, O and O2 ionization, dissociation and dissociative ionization cross sections.

(9)-(12) are coupled with electron energy conservation equations in the discharge channel and acceleration lens control volumes, which we express as

$$\frac{dU_{e,i}}{dt} = \frac{5}{2}\left(\frac{\Gamma_{e,a\to i}T_{e,a} - \Gamma_{e,i\to an}T_{e,i}}{V_i}\right) + \frac{\int n_e v_e \cdot \nabla\phi \, dV_i}{V_i}$$
$$- \beta \sum_j \nu_{e,j} k_j(T_{e,i}) n_{j,i} n_{e,i} \epsilon_j - \sum_{s+} \frac{(1-\alpha_{s+,i}) n_{s+,i}}{\tau_{s+,i}} \left[\frac{2T_{e,i}}{1-\gamma_s(T_{e,i})} + \phi_{w,i}\right], \quad (14)$$

$$\frac{dU_{e,a}}{dt} = \frac{5}{2}\left(\frac{\Gamma_{e,cat\to a}T_{e,tr} - \Gamma_{e,a\to i}T_{e,a}}{V_a}\right) + \frac{\int n_e v_e \cdot \nabla\phi\, dV_a}{V_a}$$
$$- \beta\sum_j \nu_{e,j}k_j(T_{e,a})n_{j,a}n_{e,i}\epsilon_j - \sum_{s+}\frac{(1-\alpha_{s+,a})n_{s+,a}}{\tau_{s+,a}}\left[\frac{2T_{e,a}}{1-\gamma_s(T_{e,a})} + \phi_{w,a}\right], \quad (15)$$

where v_e is the electron velocity and the electron temperature is computed as

$$T_{e,i} = \frac{2U_{e,i}}{3\sum_{s+}n_{s+,i}}, \quad (16)$$

$$T_{e,a} = \frac{2U_{e,a}}{3\sum_{s+}n_{s+,a}}, \quad (17)$$

and the four terms in the right-hand side of (14) and (15) respectively represent electron energy transport, electric field work, ionization losses, and energy losses at insulating walls. These equations contain two semi-empirical parameters: the mean energy cost per ionization event β and Bohm's anomalous diffusion coefficient α_B. β mainly accounts for excitation losses, having reported values of 3 for Hall thruster Xe discharges [28]. For what concerns the electrons coming from the cathode which trigger the thruster discharge, α_B is used to compute the electron trigger velocity $v_{e,tr}$ from the 2D magnetic and potential fields solution data as

$$v_{e,tr} = \int_{A_{out}} \bar{\bar{\mu}} \cdot \nabla\phi \cdot \frac{dA}{A_{out}}, \quad (18)$$

where A_{out} is the outlet area of the acceleration lens control volume (coinciding with the $\phi = 0.1V_D$ equipotential surface area) and $\bar{\bar{\mu}}$ is the electron mobility tensor, expressed in (3) as a function of magnetic field solution and scalar electron mobility $\mu = 1/(\alpha_B B)$. The electron fluxes Γ_e appearing in the energy transport terms are defined as follows:

- the electrons emitted by the cathode which trigger the discharge

$$\Gamma_{e,cat\to a} = V_a\sum_{s+}\frac{\alpha_{s+,a}n_{s+,a}}{\tau_{s+,a}u_{s+,a}}v_{e,tr}; \quad (19)$$

- the electrons collected by the thruster anode

$$\Gamma_{e,i\to an} = \Gamma_{e,cat\to a} + V_a\sum_{s+}\frac{\alpha_{s+,a}n_{s+,a}}{\tau_{s+,a}}; \quad (20)$$

- the electrons flowing from the acceleration lens to the discharge channel control volume

$$\Gamma_{e,a\to i} = \Gamma_{e,i\to an} - V_i\sum_{s+}\frac{\alpha_{s+,i}n_{s+,i}}{\tau_{s+,i}}. \quad (21)$$

In (15), $T_{e,tr}$ is the temperature of the electrons emitted by the cathode. The trigger electron temperature $T_{e,tr}$, usually in the order of a few eV, has small impact on the thruster behaviour. At the reference operating condition of Figures 9 and 10, output thrust and discharge current ((32) and (33)) respectively increase of +5.6% and +4.3%

as $T_{e,tr}$ is increased from 1 eV to 10 eV. For the purpose of the analyses addressed in this work, we arbitrarily set $T_{e,tr} = 4$ eV.

The electron fluxes defined in (19) to (21) allow to estimate the electric field work in the two thruster control volumes:

$$\int_{V_i} n_e v_e \cdot \nabla\phi\,\mathrm{d}V = \int_{V_i} \nabla\cdot(\phi n_e v_e)\,\mathrm{d}V - \int_{V_i} \phi\nabla\cdot(n_e v_e)\,\mathrm{d}V =$$
$$\Gamma_{e,i\to an}\phi_{an} - \Gamma_{e,a\to i}\phi_{a,in} - (\Gamma_{i,a\to an} - \Gamma_{e,a\to i})\phi_i \quad (22)$$

$$\int_{V_a} n_e v_e \cdot \nabla\phi\,\mathrm{d}V = \Gamma_{e,a\to i}\phi_{a,in} - \Gamma_{e,cat\to a}\phi_{a,out} - (\Gamma_{e,a\to i} - \Gamma_{e,cat\to a})\phi_a \quad (23)$$

where

$$\phi_i = \int_{V_i} p_i\phi\mathrm{d}V, \quad (24)$$

$$\phi_{a,in} = \int_{A_{a,in}} \phi\mathrm{d}A/A_{a,in}, \quad (25)$$

$$\phi_a = \int_{V_a} p_a\phi\mathrm{d}V, \quad (26)$$

$$\phi_{a,out} = \int_{A_{a,out}} \phi\mathrm{d}A/A_{a,out} \quad (27)$$

are computed from the 2D potential solver solution data. In (24) and (26), p_i and p_a are the probability density functions of the ion birth location in the discharge channel and acceleration lens control volume, respectively. Since the ion Monte Carlo algorithm samples the initial ion position from a uniform distribution in the two control volumes, it follows $p_i = 1/V_i$ and $p_a = 1/V_a$.

Electron energy loss at insulating walls is estimated based on the formulation derived in [39] and extended to multi-species plasma in [40]. In (14) and (15), we express the wall sheath potential Φ_w as

$$\phi_w = T_e \ln\left[\frac{v_{th,e}}{4v_B}(1 - \gamma(T_e))\right], \quad (28)$$

$$v_B = \sqrt{\sum_{s+}\frac{(1-\alpha_{s+})n_{s+}}{\tau_{s+}}\frac{eT_e}{M_s}\bigg/\sum_{s+}\frac{(1-\alpha_{s+})n_{s+}}{\tau_{s+}}}, \quad (29)$$

$$\gamma(T_e) = \sum_{s+}\frac{(1-\alpha_{s+})n_{s+}\gamma_s(T_e)}{\tau_{s+}}\bigg/\sum_{s+}\frac{(1-\alpha_{s+})n_{s+}}{\tau_{s+}}, \quad (30)$$

where v_B is a common ion sound velocity and γ is an effective secondary electron emission weighted on the ionized s-th species particle flux at the wall. The semi-empirical relation for BN secondary electron emission derived in [41] is used for $\gamma_s(T_e)$:

$$\gamma_s = \sqrt{T_e/0.35} \quad if \quad \gamma_s < 1 - 8.3\sqrt{m_e/M_s},$$
$$\gamma_s = 1 - 8.3\sqrt{m_e/M_s} \quad if \quad \gamma_s \geqslant 1 - 8.3\sqrt{m_e/M_s}. \quad (31)$$

As the ODE system represented by (9)-(12) and (14)-(15) is solved, thruster performance in terms of thrust T and discharge current I_D derive as follows:

$$T = M_s V_a \sum_{s+} \frac{\alpha_{s+,a} n_{s+,a} u_{s+,a}}{\tau_{s+,a}} + M_s V_a \sum_{s} \frac{\alpha_{s,a} n_{s,a} u_{s,a}}{\tau_{s,a}}, \tag{32}$$

$$I_D = e V_a \sum_{s+} \frac{\alpha_{s+,a} n_{s+,a}}{\tau_{s+,a}} + e V_a \sum_{s+} \frac{\alpha_{s+,a} n_{s+,a} v_{e,tr}}{\tau_{s+,a} u_{s+,a}}. \tag{33}$$

4. Results and Discussion

4.1. Model Calibration

To calibrate the model, we define the objective function

$$obj(\alpha_B, \beta) = \sum_{exp} \left[\left(\frac{T - T_{exp}}{T_{exp}} \right)^2 + \left(\frac{I_D - I_{D,exp}}{I_{D,exp}} \right)^2 \right], \tag{34}$$

where α_B and β are the anomalous diffusion and excitation cost model calibration coefficients, T_{exp} and $I_{D,exp}$ are the thrust and mean discharge current experimentally demonstrated in the verified six thruster operating conditions, and T and I_D are defined according to (32) and (33). The model is calibrated by finding the values $\alpha_{B,0}$ and β_0 which minimize the objective function.

Based on the available experimental data set, the output calibration as computed by MATLAB built-in pattern search optimization algorithm is $\alpha_{B,0} = 1/126$ and $\beta_0 = 2.77$. Even if β_0 is lower than the suggested value of 3 for Xe discharges [28], excitation losses are actually larger for atmospheric propellant as the cost coefficient multiplies for higher energy processes (such as N_2 dissociative ionization, requiring an energy of about 26.7eV as opposed to Xe single ionization energy of 12.1eV). On the other hand, the anomalous transport coefficient calibrates to $\alpha_{B,0} = 1/126$, which is consistent with the $\alpha_B = 1/100$ to $\alpha_B = 1/160$ historically used for Hall thruster Xe discharges [42]. Figure 9 shows the calibrated model solution for 20 ms duration at a reference inlet mass flow rate $\dot{m}_{N_2,in} = 3.36$ mg/s, $\dot{m}_{O_2,in} = 2.64$ mg/s and discharge voltage $V_D = 300$ V. The thruster ignition transient features a sharp peak in plasma density, followed by damped oscillations reaching steady-state in less than 3 ms. The output thrust, discharge current, anodic specific impulse and discharge power are shown in Figure 10. In the acceleration lens control volume, neutral flow composition (weighted on number density) is $0.16N_2+0.42N+0.06O_2+0.36O$, while the composition of the ion flow is $0.17N_2^++0.43N^++0.19O_2^++0.21O^+$. Table 4 reports the steady-state values of number densities in the two control volumes, together with the individual contributions to thrust T_s and discharge current I_s of the simulated species. At the simulated operating condition, the trigger electron current accounts for 13% of the total discharge current, and dissociated N^+ and O^+ ions contribute to 72% of the total ion beam current and 64% of the total thrust.
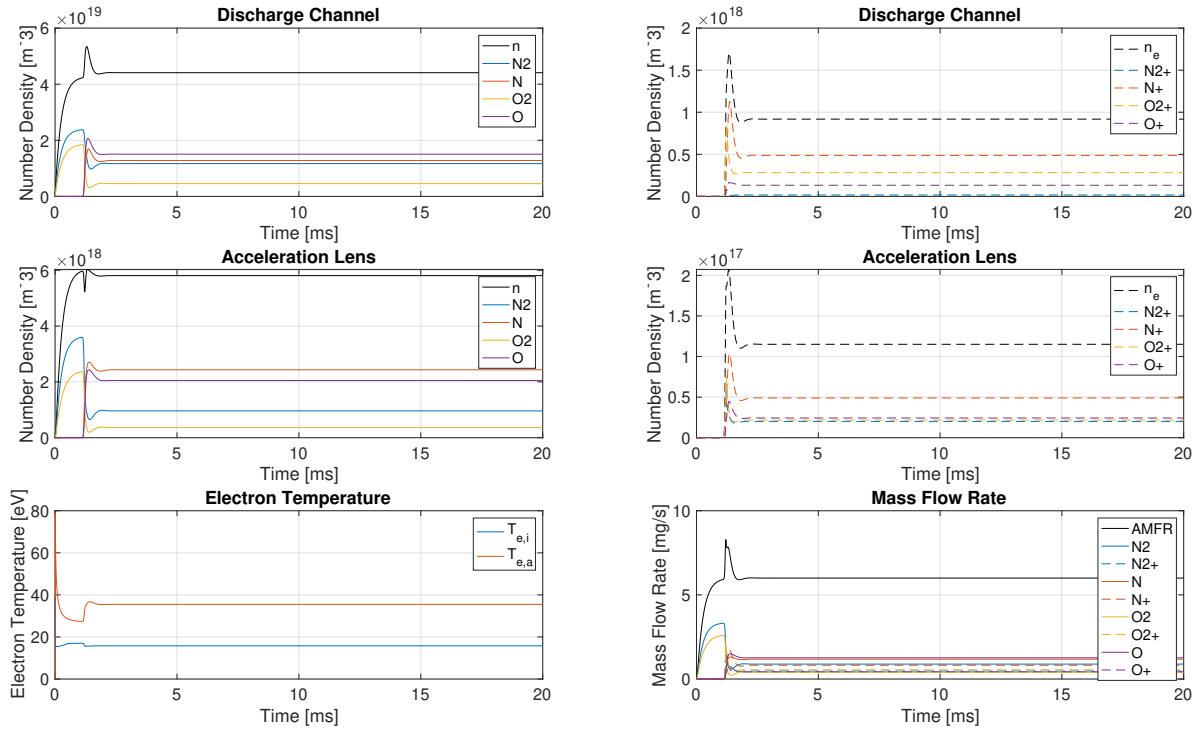
Figure 9: Ion and neutral number densities and electron energy solution at $\dot{m}_{N_2,in} = 3.36$ mg/s, $\dot{m}_{O_2,in} = 2.64$ mg/s and $V_D = 300$ V. $\beta_0 = 2.77$ and $\alpha_{B,0} = 1/126$. The mass flow rate ejected from the acceleration lens is computed as $\dot{m}_{s,out} = V_a M_s \alpha_{s,a} n_{s,a}/\tau_{s,a}$.
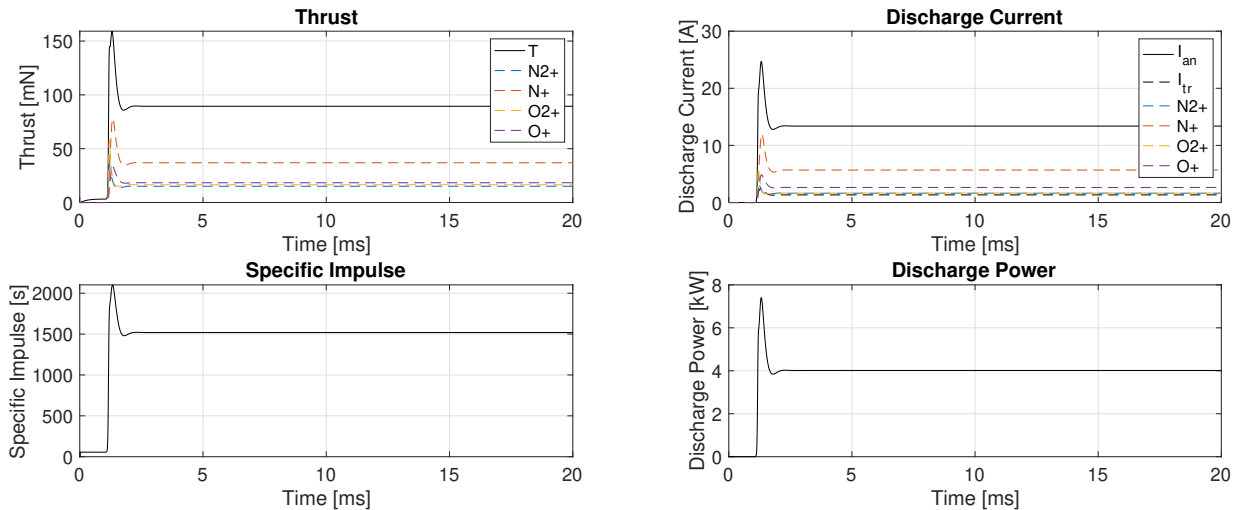

Figure 10: Ions contribution to thrust and discharge current, anodic specific impulse and discharge power at $\dot{m}_{N_2,in} = 3.36$ mg/s, $\dot{m}_{O_2,in} = 2.64$ mg/s and $V_D = 300$ V. $\beta_0 = 2.77$ and $\alpha_{B,0} = 1/126$.

Table 4: Steady-state ODE solution at $\dot{m}_{N_2,in} = 3.36$ mg/s, $\dot{m}_{O_2,in} = 2.64$ mg/s and $V_D = 300$ V. $\beta_0 = 2.77$ and $\alpha_{B,0} = 1/126$.

| Species	$n_{s,i}$ $[m^{-3}]$	$n_{s,a}$ $[m^{-3}]$	$\dot{m}_{s,out}$ $[mg/s]$	T_s $[mN]$	I_s $[A]$
N_2	1.13e19	9.11e17	0.84	0.42	0
N	1.30e19	2.43e18	1.18	0.82	0
O_2	4.36e18	3.41e17	0.37	0.18	0
O	1.52e19	2.04e18	1.26	0.81	0
N_2^+	1.76e16	2.01e16	0.47	15.1	1.63
N^+	5.23e17	5.19e16	0.87	36.9	5.68
O_2^+	2.86e17	2.19e16	0.55	16.5	1.66
O^+	1.45e17	2.57e16	0.46	18.4	2.64

4.2. Calibrated Model vs Experimental Performance

During the test, thermal and discharge stability was demonstrated for $0.56N_2+0.44O_2$ injected mass flow rate in the 5 mg/s to 7 mg/s range and at discharge voltages of 225 V and 300 V, resulting into discharge powers between 1.2 kW and 5.2 kW. During all testing activities the background pressure was always between 2e-5 mbar and 2.5e-5 mbar and, depending on the operating condition, the thruster achieved anodic efficiencies in the 10% to 20% range and specific impulses in the 600 s to 1600 s range. PFG operation seems promising for VLEO simulation on-ground, as such specific impulse levels are fairly consistent with VLEO orbital velocity of about 7.8km/s. However, while the VLEO flow would consist of neutral species (being N_2 and O the major constituents) all sharing the same collimated speed at orbital velocity, the PFG plume is instead composed of slow neutrals and very high-speed ions. This poses a limit on the actual degree of representativeness which can be achieved. As a reference, the mean exhaust velocity of each ion and neutral species for a 300 V discharge are reported in Table 2, while Table 4 includes the s-species contribution to exhaust mass flow rate at the $\dot{m}_{N_2,in} = 3.36$ mg/s, $\dot{m}_{O_2,in} = 2.64$ mg/s and $V_D = 300$ V operating condition.

The comparison among experimental data and calibrated solutions is provided in Table 5 and visualized in Figure 11. Despite the numerous approximations used in the model, the results are surprisingly accurate as a mean absolute error of 3.7%in thrust and 7.6% in discharge current (or, equivalently, discharge power) was obtained in the tested operating conditions. Main source of error is likely due to actual neutral residence times less than the one used in the simulation. Indeed, the onset of transitional flow regime near propellant injection reduce the residence time with respect to a collisionless flow, while the thruster walls thermalize neutral particles at temperatures larger than the simulated one as the discharge power is increased. The discrepancy among model and experimental results could be reduced by coupling the 0D-hybrid plasma description with a thruster thermal model, together with the integration of a collision operator in the Monte Carlo routine iterating with the number densities solved for in the 0D continuity equations. Other possible improvements relate to the modeling of additional 0D control

Table 5: Comparison among experimental data of PFG operating with $0.56N_2+0.44O_2$ inlet mass flow rate and model results for $\beta_0 = 2.77$ and $\alpha_{B,0} = 1/126$.

Operating Point		Experiments		Model		Relative Error	
V_D [V]	$\dot{m}$ [mg/s]	T [mN]	I_D [A]	T [mN]	I_D [A]	T [%]	I_D [%]
225	5	32	5.33	30.0	4.83	-6.2	-9.4
225	6	60	10.4	60.7	10.9	-1.1	+5.1
225	7	83	14.4	91.0	17.1	+9.7	+19
300	5	58	8.80	57.9	8.29	-0.2	-5.9
300	6	91	13.6	89.4	13.4	-1.7	-1.9
300	7	118	18.0	122	18.7	+3.0	+4.0
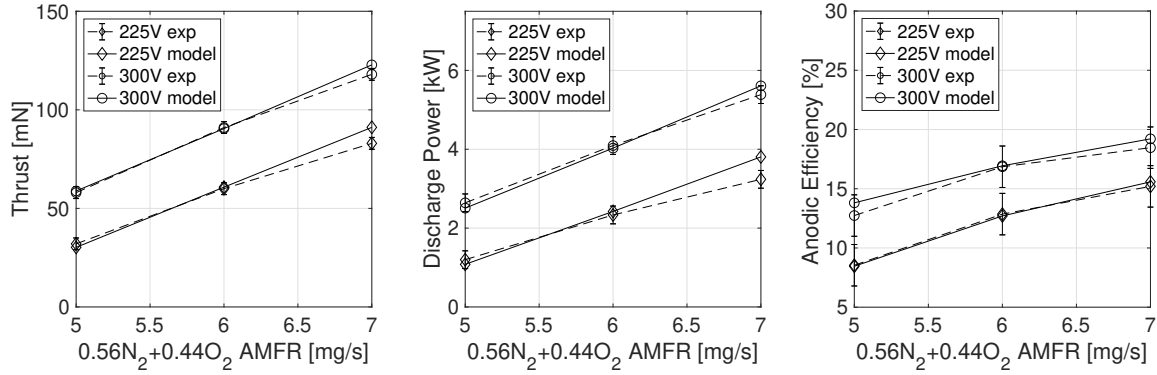
Figure 11: Comparison among verified PFG operating conditions and model results for $\beta_0 = 2.77$ and $\alpha_{B,0} = 1/126$. Discharge power and anodic efficiency are defined as $P_D = V_D I_D$ and $\eta = T^2/(2\dot{m}P_D)$.

volumes solving for the hollow cathode, thruster plume and vacuum facility coupled physics. Lastly, the explicit inclusion of excited species and chemical reactions at walls in 0D continuity and electron energy equations would provide a better description than the β calibration parameter, while more careful analysis may be dedicated to improve the modeling of electron transport, currently tuned by a constant value of the anomalous diffusion coefficient α_B.

4.3. Sensitivity to Calibration Parameters

Model sensitivity to calibration parameters is shown in Figure 12 for the reference $\dot{m}_{N_2,in} = 3.36$ mg/s, $\dot{m}_{O_2,in} = 2.64$ mg/s and $V_D = 300$ V operating condition. Thrust, power and efficiency respectively decrease from 128 mN, 6.23 kW and 22% to 75.6 mN, 3.28 kW and 14.5% when switching from $\alpha_B = 1/50$ and $\beta = 2$ to $\alpha_B = 1/150$ and $\beta = 3$. A larger value of β increases excitation losses and has a negative impact on the output thrust, power and efficiency. Larger values of α_B implies a higher electron collisionality and transport across magnetic field lines, which increase the electron trigger
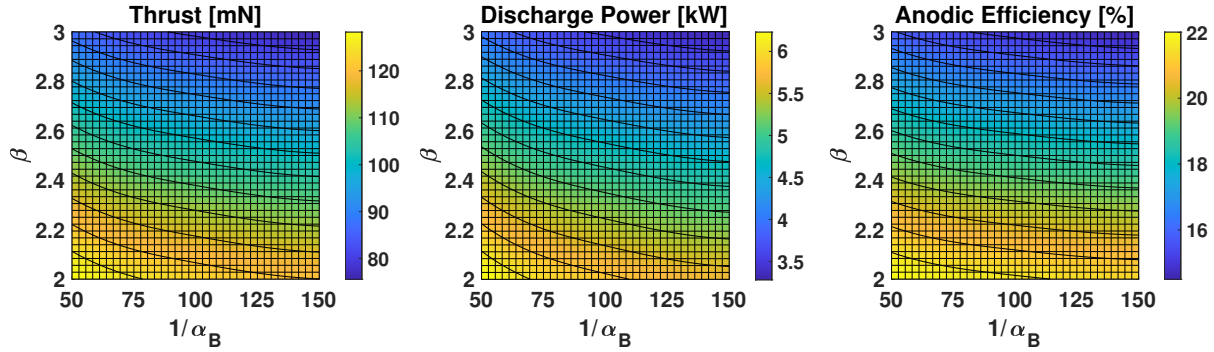
Figure 12: Model sensitivity to calibration parameters at $\dot{m}_{N_2,in}$ = 3.36 mg/s, $\dot{m}_{O_2,in}$ = 2.64 mg/s and V_D = 300 V operating condition.

velocity. The impact on performance is positive: as in calibrated condition the flow is far from being completely ionized, a larger trigger velocity improves flow ionization and increases both thrust, discharge power and anodic efficiency. As discussed in [42], the optimum value of anomalous electron transport is the minimum one ensuring complete flow ionization. Larger electron trigger velocities would only increase the discharge power with negligible impact on thrust, thus negatively affecting the anodic efficiency.

4.4. Sensitivity to Neutrals and Ions Mean Residence Time

Figure 13 shows the output thrust, discharge power and anodic efficiency obtained by varying the residence times computed from the neutral and ion Monte Carlo. A larger residence time of both ion and neutral species is beneficial, as the resulting increase in neutral and plasma density enhance ionization thus improving the thruster mass utilization efficiency. As Figure 13 shows, varying all neutral residence times from -10% to +100% increase performance from 73.4 mN, 3.18 kW and 14.1% to 175 mN, 8.58 kW and 29.6%, respectively. A variation from -10% to +100% in all ion residence times
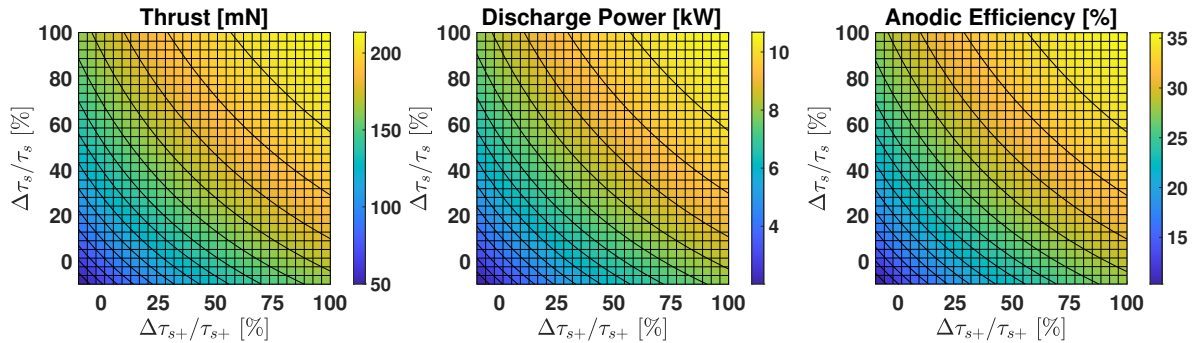

Figure 13: Model sensitivity to neutral and ion residence time variation in the -10% to +100% range. The operating condition is fixed at $\dot{m}_{N_2,in}$ = 3.36 mg/s, $\dot{m}_{O_2,in}$ = 2.64 mg/s and V_D = 300. α_B = 1/126 and β = 2.77.

leads to an equivalent result. When both ion and neutral residence times are increased of +100%, 213 mN of thrust, 8.88 kW of discharge power, and 35.6% of anodic efficiency are achieved. In this regard, a propellant injection scheme favouring neutral residence in the channel could improve performance.

4.5. Sensitivity to Inlet Mass Flow Rate and Discharge Voltage

Figure 14 shows model sensitivity to inlet mass flow rate (at the reference $0.56N_2+0.44O_2$ composition) in the 4 mg/s to 8 mg/s range and discharge voltage in the 300 V to 600 V range.
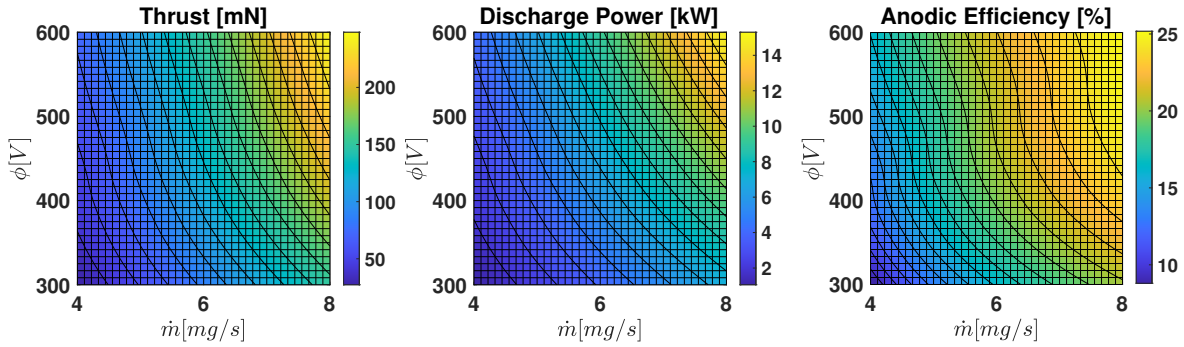

Figure 14: Model sensitivity to inlet mass flow rate and discharge voltage at a fixed $0.56N_2+0.44O_2$ inlet composition. $\alpha_B = 1/126$ and $\beta = 2.77$.

As the provided results are not supported by experimental evidence, actual performance may deviate significantly from the one presented here, mainly due to variations in the particles excitation state or electron anomalous diffusion (which may give rise to a different calibration value for the β cost factor and α_B coefficient) and to an increase in channel and anode temperature (which reduces the neutrals residence time) when operating at large discharge power levels. Nonetheless, the output performance map is consistent with the typical behaviour of Hall thruster operating with traditional Xe propellant as both thrust, discharge power and anodic efficiency increase with mass flow rate and discharge voltage. 248 mN, 15.3 kW and 25% of thrust, discharge power and anodic efficiency are achieved at $\dot{m}_{in} = 8$ mg/s and $V_D = 600$ V as compared to the output 27.3 mN, 1.06 kW and 8.8% at $\dot{m}_{in} = 4$ mg/s and $V_D = 300$ V.

4.6. Sensitivity to Inlet Flow Composition

Impact of flow composition on thrust, discharge power and anodic efficiency is visualized in Figure 15. Since nitrogen and oxygen can only be stored in molecular form for on-ground testing and considering that atomic oxygen is, together with N_2, the main constituent of the upper atmosphere, we plot the impact of N_2, O_2 and O inlet mass flow rate fractions at a reference $V_D = 300$ V and $\dot{m}_{in} = 6$ mg/s operating condition. The x-axes of Figure 15 represents the transition from pure N_2 to pure O_2 injected propellant. Due to the higher likelihood and energy required to dissociate N_2 with
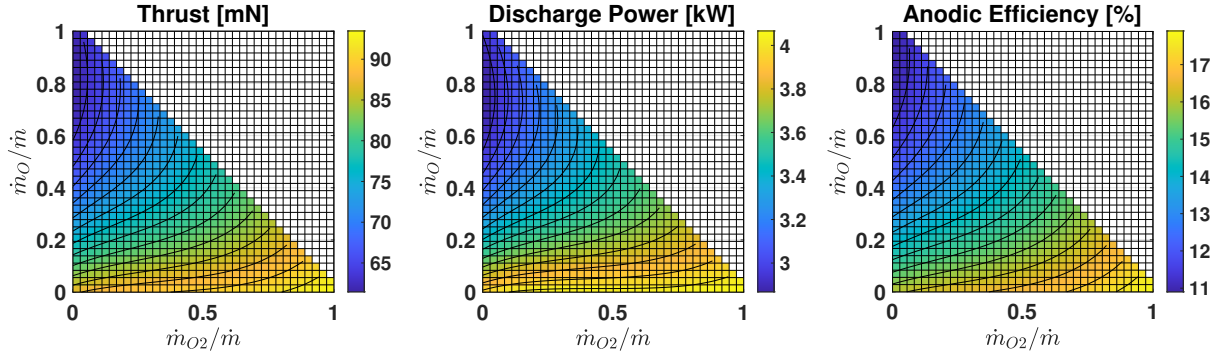
Figure 15: Model sensitivity to inlet N_2, O_2 and O inlet composition at fixed $\dot{m}_{in} = 6$ mg/s and $V_D = 300$ V operating condition. $\alpha_B = 1/126$ and $\beta = 2.77$. The graph origin corresponds to a pure N_2 inlet mass flow.

respect to O_2, thrust, discharge power and anodic efficiency respectively increase from 86.6 mN, 3.93 kW and 16% to 93.5 mN, 4.07 kW and 18% when switching from N_2 to O_2 propellant. Even if no dissociation energy losses occur for pure O, thrust, discharge power and efficiency respectively reduce to 62.3 mN, 2.96 kW and 11% when operating with atomic oxygen only. This is likely due to the lower residence time of atomic oxygen as compared to molecular species, which negatively impacts the ionization efficiency of the thruster. Since most of the inlet N_2 and O_2 molecules are dissociated in the discharge, the variation in output thrust and discharge power is less than expected when switching from molecular to atomic propellant. Indeed, the solution of Figure 10 for the reference operating condition $\dot{m}_{N_2,in} = 3.36$ mg/s, $\dot{m}_{O_2,in} = 2.64$ mg/s and $V_D = 300$ V shows how dissociated N^+ and O^+ ions contribute to a significant 64% of the total thrust and 72% of the total ion beam current.

5. Conclusions

In November 2021, the HT5k 5kW-class Hall thruster was successfully characterized with atmospheric propellant. To the best of the authors knowledge, this was the first verification of an air-fed, magnetically shielded Hall thruster coupled with a nitrogen fed hollow cathode. Thruster performance and plume properties were characterized in six operating conditions ranging from 5 mg/s to 7 mg/s of injected $0.56N_2 + 0.44O_2$ mass flow rate and at 225 V and 300 V of discharge voltage. In all points tested the discharge current signal was very stable, and the used power supply was always capable of sustaining the discharge load. The verified thruster performance ranged between 30 mN to 120 mN of thrust, 1.2 kW to 5.2 kW of discharge power, and 8% to 18% of anodic efficiency. The measured performance were compared with the solution of the 0D-hybrid model presented in this work. The model formulation was developed in [19] for an air-breathing EP prototype, adapted here to a traditional Hall thruster discharge, and calibrated against the six verified operating conditions by tuning an anomalous electron

diffusion coefficient and an effective ionization cost parameter. Despite the several assumptions used, the calibrated model output resulted into a mean absolute error of 3.7% in thrust and 7.6% in discharge power. Model sensitivity to calibration parameters, ion and neutral particles residence time, operating condition and inlet flow composition was also presented and discussed. Possible improvements relate to the possibility of coupling it with a thruster thermal model, to include a Monte Carlo collision operator, and to add additional domain regions including hollow cathode, plume, and vacuum facility control volumes.

Acknowledgement

References

[1] N.H. Crisp et al. "System modelling of very low Earth orbit satellites for Earth observation", Acta Astronautica 187 (2021) 475–491, doi:10.1016/j.actaastro.2021.07.004

[2] N.H. Crisp et al., "The benefits of very low earth orbit for earth observation missions", Progress in Aerospace Sciences Volume 117, August 2020, 100619, doi:10.1016/j.paerosci.2020.100619

[3] Berthoud, L., Hills, R., Bacon, A. et al. Are Very Low Earth Orbit (VLEO) satellites a solution for tomorrow's telecommunication needs?. CEAS Space J (2022). doi:10.1007/s12567-022-00437-0

[4] Tony Schönherr et al, "Analysis of Atmosphere-Breathing Electric Propulsion", IEEE Transactions on Plasma Science (Volume: 43, Issue: 1, Jan. 2015), doi:10.1109/TPS.2014.2364053

[5] M. Tagawa, K. Yokota, K. Nishiyama, H. Kuninaka, Yasuo Yoshizawa, Daisaku Yamamoto, Takaho Tsuboi, "Experimental Study of Air Breathing Ion Engine Using Laser Detonation Beam Source", Journal of Propulsion and Power vol. 28 Iss. 3, 2013, DOI:10.2514/1.B34530.

[6] Erofeev, A. I.; Nikiforov, A. P.; Popov, G. A.; Suvorov, M. O.; Syrin, S. A.; Khartov, S. A., "Air-Breathing Ramjet Electric Propulsion for Controlling Low-Orbit Spacecraft Motion to Compensate for Aerodynamic Drag", Solar System Research, Volume 51, Issue 7, pp.639-645, 2017, doi: 10.1134/S0038094617070048

[7] T. Andreussi, E. Ferrato, A. Piragino, V. Giannetti, C.A. Paissoni, M. Andrenucci, "Development Status and Way Forward of SITAEL Air-breathing Electric Propulsion Engine", AIAA Propulsion and Energy Forum Exposition, August 2019, Indianapolis (US), doi: 10.2514/6.2019-3995

[8] F. Romano et al, "RF Helicon-based Inductive Plasma Thruster (IPT) Design for an Atmosphere-Breathing Electric Propulsion system (ABEP)", November 2020 Acta Astronautica 176C:476-483, doi:10.1016/j.actaastro.2020.07.008.

[9] Peng Zheng , Jianjun Wu , Yu Zhang, and Biqi Wu, "A Comprehensive Review of Atmosphere-Breathing Electric Propulsion Systems", International Journal of Aerospace Engineering, Volume 2020 Article ID 8811847, 2020, doi:10.1155/2020/8811847.

[10] G. Cifali, T. Misuri, P. Rossetti, M. Andrenucci, D. Valentian, D. Feili and B. Lotz "Experimental Characterization of HET and RIT with Atmospheric Propellants", IEPC-2011-224, 2011

[11] Antonio Gurciullo, Andrea Lucca Fabris, and Mark A Cappelli, "Ion plume investigation of a Hall

effect thruster operating with Xe/N2 and Xe/air mixtures", 2019 J. Phys. D: Appl. Phys. 52 464003.

[12] Semenkin, A. V., et al., "Study of anode layer thruster operation with gas mixtures", IEPC 95-78.

[13] A. I. Erofeeva, A. P. Nikiforova, G. A. Popovb, M. O. Suvorovb,S. A. Syrinb, and S. A. Khartovb, "Air-Breathing Ramjet Electric Propulsion for Controlling Low-Orbit Spacecraft Motion to Compensate for Aerodynamic Drag", December 2017, Solar System Research 51(7):639-645, doi:10.1134/S0038094617070048

[14] F. Romano, Y. Chan, G. Herdrich, C. Traub, and P. Roberts, "Design, Set-Up, and First Ignition of the RF Helicon-based Plasma Thruster", Space Propulsion Conference 2020+1Volume: 00247, March 2021.

[15] Charles, Christine, et al. "An experimental investigation of alternative propellants for the helicon double layer thruster". Journal of Physics D: Applied Physics 1.17 (2008): 175213.

[16] L. Guarrigues, "Computational Study of Hall-Effect Thruster with Ambient Atmospheric Gas as Propellant", Journal of Propulsion and Power, Vol. 28, No. 2, March-April 2012, DOI:10.2514/1.B34307

[17] Taploo, A., Lin, L., Keidar, M. (2021). Analysis of ionization in air-breathing plasma thruster. Physics of Plasmas, 28(9). https://doi.org/10.1063/5.0059896

[18] Mrozek, K., Dytrych, T., Moliš, P., Daniel, V., Obrusnik, A. (2021), "Global plasma modeling of a magnetized high-frequency plasma source in low-pressure nitrogen and oxygen for air-breathing electric propulsion applications". Plasma Sources Science and Technology, 30(12). https://doi.org/10.1088/1361-6595/ac36ac

[19] Ferrato, E., Giannetti, V., Tisaev, M., Lucca Fabris, A., Califano, F., and Andreussi, T., "Rarefied Flow Simulation of Conical Intake and Plasma Thruster for Very Low Earth Orbit Spaceflight", Frontiers in Physics, 2022. doi: 10.3389/fphy.2022.833159.

[20] M. Tisaev, E. Ferrato, V. Giannetti, C.A. Paissoni, N. Baresi, A. Lucca Fabris, and T. Andreussi "Air-breathing electric propulsion: flight envelope identification and development of control for long-term orbital stability", Acta Astronautica, Volume 191, February 2022, Pages 374-393, doi:10.1016/j.actaastro.2021.11.011.

[21] V. Giannetti, E. Ferrato, A. Piragino, M. Reza, F. Faraji, M. Andrenucci and T. Andreussi, "HT5k Thruster Unit Development History, Status and Way Forward", IEPC-2019-878, 36th International Electric Propulsion Conference University of Vienna, Austria 2019

[22] T. Andreussi et al. "The AETHER Project: development of air-breathing electric propulsion for VLEO missions", 1st International Symposium on Very Low Earth Orbit Missions and Technologies, accepted for publication in CEAS Space Journal.

[23] Pedrini, D.; Misuri, T.; Paganucci, F.; Andrenucci, M. Development of Hollow Cathodes for Space Electric Propulsion at Sitael. Aerospace 2017, 4, 26. https://doi.org/10.3390/aerospace4020026

[24] James E. Polk, Anthony Pancotti, Thomas Haag, Scott King, Mitchell Walker, Joseph Blakely and John Ziemer, "Recommended Practice for Thrust Measurement in Electric Propulsion Testing", Journal of Propulsion and Power, Volume 33, Number 3, May 2017, doi:10.2514/1.B35564.

[25] Kentaro Hara, "An overview of discharge plasma modeling for Hall effect thrusters", 2019 Plasma Sources Sci. Technol. 28 044001, doi:10.1088/1361-6595/ab0f70

[26] J.P. Boeuf, "Tutorial: Physics and modeling of Hall thrusters", Journal of Applied Physics 121, 011101 (2017), DOI:10.1063/1.4972269.

[27] Hecht, F.. "New development in freefem++" Journal of Numerical Mathematics, vol. 20, no. 3-4, 2012, pp. 251-266. doi:10.1515/jnum-2012-0013

[28] M. Keidar and I. D. Boyd, "Plasma flow and plasma–wall transition in Hall thruster channel", Physics of Plasmas 8, 5315 (2001); https://doi.org/10.1063/1.1421370

[29] I. Katz, I.G. Mikellides, B.A. Jorns and A.L. Ortega, "Hall2De Simulations with an Anomalous Transport model Based on the Electron Cyclotron Drift Instability", IEPC-2015-402 / ISTS-2015-b-402, Presented at Joint Conference of 30th International Symposium on Space Technology and Science 34th International Electric Propulsion Conference and 6th Nano-satellite Symposium,

Hyogo-Kobe, Japan July 4 – 10, 2015.

[30] S. Livadotti et al., "A review of gas-surface interaction models for orbital aerodynamics applications", Progress in Aerospace Sciences 119 (2020) 100675, doi:10.1016/j.paerosci.2020.100675

[31] Jose F. Padilla and Iain D. Boyd, "Assessment of Gas–Surface Interaction Models for Computation of Rarefied Hypersonic Flow", Journal of Thermophysics and Heat Transfer, University of Michigan, Ann Arbor, Michigan 48109 January–March 2009 doi:10.2514/1.36375

[32] C.K. Birdsall, A.B Langdon "Plasma Physics via Computer Simulation", CRC Press, 2004. doi:10.1201/9781315275048

[33] Geng, J, Brieda L., Rose, L. and Keidar M. "On applicability of the "thermalized potential" solver in simulations of the plasma flow in Hall thrusters" Journal of Applied Physics 114, 103305 (2013); doi: 10.1063/1.4821018

[34] I. G. Mikellides, I. Katz, R. R. Hofer, and D. M. Goebel, "Magnetic shielding of a laboratory Hall thruster. I. Theory and validation", Journal of Applied Physics 115, 043303 (2014); https://doi.org/10.1063/1.4862313.

[35] W. Hwang and Y.-K. Kim, "New model for electron-impact ionization cross sections of molecules" J. Chem. Phys. 104, 2956 (1996); https://doi.org/10.1063/1.471116

[36] Yong-Ki Kim and Jean-Paul Desclaux, "Ionization of carbon, nitrogen, and oxygen by electron impact" Phys. Rev. A 66, 012708 – Published 19 July 2002; doi.org/10.1103/PhysRevA.66.012708

[37] P. C. Cosby, "Electron Impact Dissociation of Nitrogen" J. Chem. Phys. 98, 9544 (1993); https://doi.org/10.1063/1.464385

[38] D. Rapp, P. Englander-Golden, and D. D. Briglia, "Electron Impact Dissociation of Nitrogen" J. Chem. Phys. 42, 4081 (1965); https://doi.org/10.1063/1.1695897

[39] E. Ahedo, "Presheath/sheath model with secondary electron emission from two parallel walls", Physics of Plasmas 9, 4340 (2002); https://doi.org/10.1063/1.1503798

[40] D. Lee, L. Oksuz, and N. Hershkowitz, "Exact solution for the generalized Bohm criterion in a two-ion-species plasma," Physical review letters, vol. 99, no. 15, p. 155004, 2007.

[41] A. Dunaevsky, Y. Raitses, and N. J. Fisch, "Secondary electron emission from dielectric materials of a Hall thruster with segmented electrodes", Physics of Plasmas 10, 2574 (2003); https://doi.org/10.1063/1.1568344

[42] K. Kwon, M.L.R. Walker, and D.N. MAvris, "Study on Anomalous Electron Diffusion in the Hall Effect Thruster", International Journal of Aeronautical and Space Sciences, 15(3), 112–121 (2014); DOI:10.5139/IJASS.2014.15.3.23